Characterization of a Cadmium Capture-gated Neutron Spectrometer

Nathaniel John Hogan

A senior thesis submitted to the faculty of
Brigham Young University
in partial fulfillment of the requirements for the degree of

Bachelor of Science

Lawrence Rees, Advisor

Department of Physics and Astronomy

Brigham Young University

August 2011

ABSTRACT

Characterization of a Cadmium Capture-gated Neutron Spectrometer

Nathaniel John Hogan
Department of Physics and Astronomy
Bachelor of Science

The characterization of a newly developed capture-gated neutron spectrometer is presented. Such spectrometers produce a dual signal from incoming neutrons, allowing for differentiation between other particles, particularly gamma rays. The neutron provides a primary light pulse in either plastic or liquid scintillator through neutron-proton collisions. A capture material then captures the moderated neutron exciting the material. The capture material promptly de-excites with the emission of gamma rays, which then produces a second pulse. The present spectrometer alternates one-centimeter thick plastic scintillators with sheets of cadmium inserted in between for neutron capture. Each neutron captured in cadmium releases about 9 MeV of gamma energy.

Many factors influence the operation of the spectrometer, including: materials, geometry, optics, and methods of analysis. Experiments are presented that weigh the effect that these factors have on the capabilities of the detector. Theoretical, computational and experimental data presented here also illustrates the detector's ability to be utilized in applications of neutron detection for nuclear non-proliferation. The intrinsic efficiency of the detector for the detection of spontaneous fission neutrons from ^{252}Cf is measured to be 5.23%.

Keywords: neutron, capture-gated

ACKNOWLEDGMENTS

Tomu’a tuku ha fakamalo ki he Tamai Hevani. Many thanks to Dr. Rees and Dr. Czirr for taking an exorbitant amount of time answering my never-ending train of questions, and for giving me the chance to excel. To you two, I will always be indebted. Thanks to Adam Wallace who spent so much of his own research time helping me understand my programming errors.

Parts of this work were funded by NNSA Grant no. DE-FG52-10NA29655 and DHS Award no. 2010-DN-077-ARI039-02.

Contents

Table of Contents **iv**

1 Introduction **1**
- 1.1 Motivation and Applications . . . 1
- 1.2 An Introduction to Neutron Detection . . . 2
- 1.3 The Capture-gated Method . . . 4
- 1.4 Cross Sections . . . 6
- 1.5 Compton Scattering . . . 7
- 1.6 Photomultiplier Tubes . . . 13
  - 1.6.1 Theory . . . 13
  - 1.6.2 A Quick Example . . . 15

2 Detector Design **20**
- 2.1 An Introduction to Monte Carlo for Neutral Particles . . . 21
- 2.2 Computaional Methods . . . 21
- 2.3 Results . . . 22
- 2.4 Design Conclusions . . . 24

3 Detector Characterization **26**
- 3.1 Characterization Introduction . . . 26
- 3.2 Results . . . 27
- 3.3 Analysis and Discussion . . . 32

4 Neutron Detection Capabilities **34**
- 4.1 Introduction . . . 34
- 4.2 Experimental Setup . . . 41
- 4.3 Results . . . 42
- 4.4 Analysis and Discussion . . . 45

5 Conclusions and Future Work **47**

Bibliography **49**

Chapter 1

Introduction

1.1 Motivation and Applications

The discovery of the neutron by Chadwick in 1932 has caused an ever-growing interest in novel neutron detection methods. Such interest exists because of the fundamental importance of neutrons in understanding the structure of the atomic nucleus. As an example, our incomplete understanding of the strong nuclear force demands novel detection methods to improve the measurement neutron-neutron and neutron-proton interactions. Such fundamental research continues to drive innovation in neutron detection.

The discovery of nuclear weapons and their rapid proliferation further accelerated the interest in neutron detection. The interdiction of the transportation and use of nuclear weapons materials requires neutron detectors for the detection of plutonium and uranium. ^{3}He detectors have been used extensively for this purpose, but a recent shortage in ^{3}He has caused an increased demand for detectors. Furthermore, this shortage of ^{3}He has caused a pinch in supply for a variety of other applications where it is employed. Consequently, developing new detection methods for nuclear grade materials will inevitably liberate ^{3}He for use in such applications [2].

I present a new method for neutron detection that can be employed in a wide variety of applications in both the scientific and applied science/engineering realms. The focus of this paper is three-fold: first, I discuss the theory and subsequent design of the detector; second, I present a series of experiments/results that characterize the detector; lastly, I present an ideal method for the detection of plutonium in nuclear non-proliferation settings.

1.2 An Introduction to Neutron Detection

Like all neutral particles, neutrons are difficult to detect directly. Thus, an indirect detection of the neutron commonly occurs by manipulating the neutron to create charged particles with detectable energies. Neutron detection is often achieved by imparting kinetic energy from the neutron to a charged particle. The simple detection of electrons ejected from a material by high energy photons is a simple example of this process: a neutral particle ejects a charged particle with sufficient kinetic energy to be detected. The analogous method for neutron detection involves collisions between neutrons and protons (n-p collisions). These collisions transfer part of the kinetic energy of the neutron to detectable proton kinetic energy.

Another common method for neutral particle detection utilizes the capture by an atomic nucleus. A number of materials exist with high neutron-capture cross sections (see Sec. 1.4 for cross sections). This capture of a neutron then directly or indirectly provides a charged particle that is subsequently detected. The type of decay mode depends on the capture nucleus. Given below is a partial list of these type of reactions.

$$\mathrm{n} + {}^{6}\mathrm{Li} \rightarrow \alpha + {}^{3}\mathrm{H} \tag{1.1}$$

$$\mathrm{n} + {}^{3}\mathrm{He} \rightarrow \mathrm{H}^{+} + {}^{3}\mathrm{H} \tag{1.2}$$

$$\mathrm{n} + {}^{10}\mathrm{B} \rightarrow \alpha + {}^{7}\mathrm{Li} \tag{1.3}$$

$$\mathrm{n} + {}^{113}\mathrm{Cd} \rightarrow {}^{114}\mathrm{Cd}^{*} \rightarrow {}^{114}\mathrm{Cd} + \gamma \tag{1.4}$$

$$\mathrm{n} + {}^{157}\mathrm{Gd} \rightarrow {}^{158}\mathrm{Cd}^{*} \rightarrow {}^{158}\mathrm{Cd} + \gamma \tag{1.5}$$

The first three reactions, involving lithium, helium and boron, leave two positively charged in the final state. The second two reactions, involving cadmium and gadolinium, produce gamma rays when the excited nucleus decays to its ground state. These gamma rays then scatter electrons for detection.

The methods for detection of these emitted charged particles are even more varied than the methods for their creation. I will review one of these methods in detail here, as it is the most relevant to the detector in question. This method utilizes a scintillating material and a photomultiplier tube (PMT). Scintillators are engineered to convert the kinetic energy of a charged particle into photons. The molecules in the scintillator accomplish this as the charged particle interacts with molecular electrons. The exchange of energy excites the electrons in the molecule. Upon de-excitation back to the molecular ground state, photons are released. The number of photons released is proportional to the energy deposited in the scintillator. Scintillators are engineered so that certain parameters fit desired experimental measurements. Such parameters include, but are not limited to, light output spectrum, decay time, absorption spectrum, refractive index, and hydrogen to carbon ratio. Scintillating materials come in many forms, including glass, plastic, or liquid, organic or inorganic.

After the scintillator emits photons they propagate inside the detector volume (usually surrounded by reflective coating) until they reach the PMT. The PMT serves to convert photons into a detectable electric voltage. (A description of this process is given in Sec. 1.6 of this chapter). This voltage can then be analyzed using either digital or analog methods.

1.3 The Capture-gated Method

The method of utilizing scintillators for detection of neutrons presents an unfortunate limitation: any charged particle traveling through the scintillator will cause light to be emitted. This poses a problem mainly because of gamma rays that Compton scattering in the scintillator, accelerating electrons through the material. These electrons generate a similar light pulse to scattered protons from n-p collisions. If we plan on detecting the charged particles from neutron capture reactions using scintillators, the same difficulty arises. Several methods strive to overcome this predicament so as to differentiate pulses caused by neutrons from those caused by other particles.

The detector presented here employs a method known as the capture-gated method. This method incorporates both n-p collisions and neutron capture. As a neutron enters the detector volume, it creates a primary light pulse in the scintillator due to multiple n-p collisions. These collisions moderate the neutron (decreasing the neutron's kinetic energy). This primary pulse will be referred to as the proton-recoil pulse. As the neutron slows down in the scintillator the probability of capture within the capture material rises. The capture reaction then releases its direct or indirect charged particles that scatter in the scintillator causing a secondary light pulse, which will be referred to as the capture pulse. This dual pulse signature differentiates neutrons from other particles that only create single pulses in the scintillator. Furthermore, the pulse-height of the primary pulse is roughly proportional to the energy of the neutron, giving this detector spectroscopic capabilities as well.

There exist important variables unique to the capture-gated method that must be considered depending on the intended application. There are also variables, however, that must be considered globally. Perhaps the two most important of these are capture efficiency and mean capture time. There is little need to expound the need for efficiency, but the importance of mean capture time is more subtle. The mean capture time is defined as the amount of time it takes 1/e of N neutrons from a fission source to capture within the material. This value obviously depends on the material used, but the geometry of the detector also plays a large role. For most applications the mean capture time should be minimized. This allows for less probability of misidentifying dual pulse signatures.

Quantifying this phenomenon requires some assumptions. As will be shown, the accidental rate is dependent on the strength of the source, or simply upon the flux of particles incident upon the detector. Assume a rate of R non-neutron particles incident on the detector per second. Then the probability of getting a single count within a certain time ΔT in seconds is given by:

$$\mathrm{P}_1 = \mathrm{R}\Delta\mathrm{T} \tag{1.6}$$

The probability of getting two counts in this same ΔT is:

$$\mathrm{P}_2 = \mathrm{R}^2\Delta\mathrm{T}^2 \tag{1.7}$$

Consider, for example, a gamma source that illuminates the detector with 5000 gammas per second. If we consider a time window of 1μs (ΔT), then R is .005 gammas per μs, and P1 = .005 and P2 = .000025.

Like any other method, the capture-gated method has disadvantages. Very active radioactive sources can blind the detector by causing accidental dual pulse signatures. Also, low energy neutrons may not create a sufficiently large primary pulse. This paper will also explore remedies to these disadvantages. Despite these challenges, the capture-gated method is a versatile and viable method.

1.4 Cross Sections

We can begin to understand cross sections with an easy classical analogue. The goal is to find the probability that a projectile will interact with a solid target of cross sectional area σ. Assume that the projectile is accurate up to $\pm\theta$, where θ is some angle. Let's also assume that any angle within this angular window is equally probable. This produces an area A into which the projectile will travel at any given distance d. This area A is given by:

$$\mathrm{A} = \pi \mathrm{d}^2 \tan^2\theta \tag{1.8}$$

So, to find the probability of hitting the target at any distance d, we simply divide the cross sectional area of the target by the area A. This gives:

$$\mathrm{P} = \frac{\sigma}{\mathrm{A}^2} \tag{1.9}$$

Certain materials have notably high neutron capture cross sections for low energy neutrons, as noted earlier. For instance, for neutrons at thermal energy, a ^{113}Cd nucleus has a capture cross section σ of 20,000 ± 300 barns. One barn equals $10^{-28}\mathrm{m}^2$. To get a feeling for what this value means, consider a thin sheet of cadmium that has an area density σ_{Cd} of ^{113}Cd atoms. We project a beam of thermal neutrons with a flux of ϕ, in units of neutron per unit time, upon the cadmium foil. We can use these values to find the number of neutrons per unit time that are absorbed:

$$N = \sigma_{Cd}\sigma\phi \tag{1.10}$$

The cross section may depend on a host of parameters, including the energy of the incident particle. For the case of cadmium, the cross section is small for neutrons with energies larger than thermal energy.

One important formalization is the idea of differential cross section, which is useful in experiments where the particle is scattered off of a target. An example of such a reaction is Compton scattering between gamma rays and electrons. The differential cross section is defined as the number of particles scattered into an infinitesimal angle dΩ divided by the total number of particles scattered and by d$^{\Omega}$, and is denoted by $\frac{d\sigma}{d\Omega}$. It is often more convenient to begin by defining the differential cross section, as it is often the directly measured quantity.

1.5 Compton Scattering

Compton scattering is important in virtually all detector systems because of the ever-present gamma background. Gamma sources also become crucial tools in characterizing and calibrating detector systems. Monoenergetic and quasi monoenergetic sources can be used if the detector's signal is proportional to the incident gamma energy, which is true in almost all cases, but is definitely true in the case of the detector in question.

Compton scattering occurs when a high energy photon of energy E_γ interacts with an electron, free or bound. This interaction can be thought of as a collision where the electron gains kinetic energy and the photon energy is reduced to E_{γ^*}. The energy of the scattered photon is given by the formula:

$$E_{\gamma^*} = \frac{E_\gamma}{1 + E_\gamma \frac{(1-\cos\theta)}{m_e c^2}} \tag{1.11}$$

where θ is the scattering angle, m_e is the electron mass, and c is the speed of light. The energy of the scattering electron is then:

$$E = E_\gamma - E_{\gamma^*} \tag{1.12}$$

The electron energy is the important quantity here because that is what manifests itself in the detector. Fig. 1.1 shows the energy of the scattering electron as a function of the scattering angle θ for some well-known values of E_γ.

This tells us nothing about the probability of Compton scattering at each angle θ. For this information we have to turn to quantum electrodynamics. The Klein-Nishina formula [3] gives the

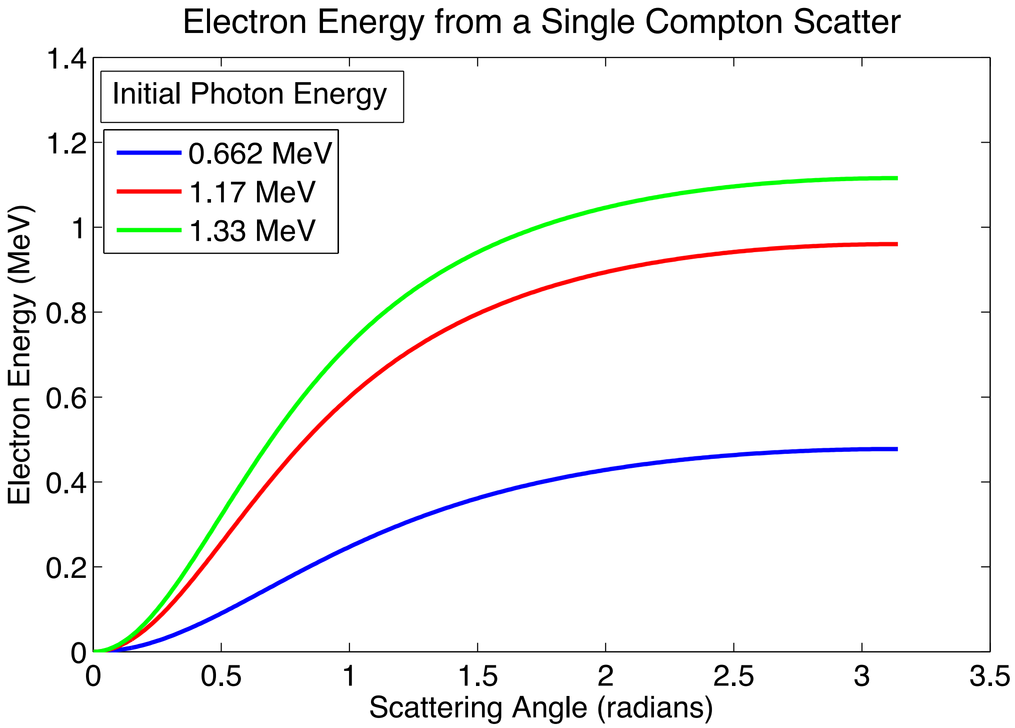

Figure 1.1 The energy of the scattering electron from Compton scattering as a function of angle for select initial photon energies

differential cross section for scattered gamma rays in Compton scattering, which can then be used to arrive at the angular distribution:

$$\frac{\mathrm{d}\sigma}{\mathrm{d}\Omega} = \mathrm{Zr}_0^2 \left(\frac{1}{1+\alpha\,(1-\cos\theta)} \right)^2 \left(\frac{1+\cos^2\theta}{2} \right) \left(1 + \frac{\alpha^2\,(1-cos\theta)^2}{(1+\cos^2\theta)\,(1+\alpha\,(1-\cos\theta))} \right) \tag{1.13}$$

$$\alpha = \frac{\mathrm{e}}{\mathrm{m}_e} \tag{1.14}$$

where m_e is the electron mass, r_0 is the classical electron radius and e is the energy of the initial gamma ray. Because this does not depend on ϕ, we can integrate with respect to ϕ and get:

$$\frac{\mathrm{d}\sigma}{\mathrm{d}\theta} = \frac{\pi \mathrm{r}_0^2 \mathrm{Z} \sin\theta \left(\cos^2\theta + 1\right) \left(\frac{\alpha^2[1-\cos\theta]^2}{\left(\cos^2\theta+1\right)[\alpha(1-\cos\theta)+1]} + 1 \right)}{[\alpha\,(1-\cos\theta)+1]^2} \tag{1.15}$$

Fig. 1.2 shows this plotted as a function of θ, for the same initial photon energies plotted before.

Now that we have the angular distribution and the electron and scattered gamma ray energy distribution as a function of angle we can calculate the energy distribution of single Compton scattering. Consider a large number N of gammas that scatter within a detector volume. The electron energy distribution gives the number of gammas that deposit an energy E. The Monte Carlo method is the simplest for obtaining these data. This distribution is plotted in Fig. 1.3, for the same initial gamma energies shown above.

It is important to note that in a single Compton scatter the electron cannot obtain all of the gamma energy. The energy peaks present in Fig. 1.3 represent the energy of the electron when the gamma scattered at an angle of $\theta = \pi$, giving a maximum electron energy of:

$$\mathrm{E} = \mathrm{E}_\gamma - \frac{\mathrm{E}_\gamma}{1+\frac{2\mathrm{E}_\gamma}{\mathrm{m}_e \mathrm{c}^2}} \tag{1.16}$$

If a detector volume is large enough, multiple Compton scattering events can occur. Monte Carlo methods can be used to calculate their contribution to the distribution. However, the variables involved depend on the detector material and volume, and a description of the process is beyond the scope of this paper. A qualitative understanding of the effect is sufficient. Multiple Compton

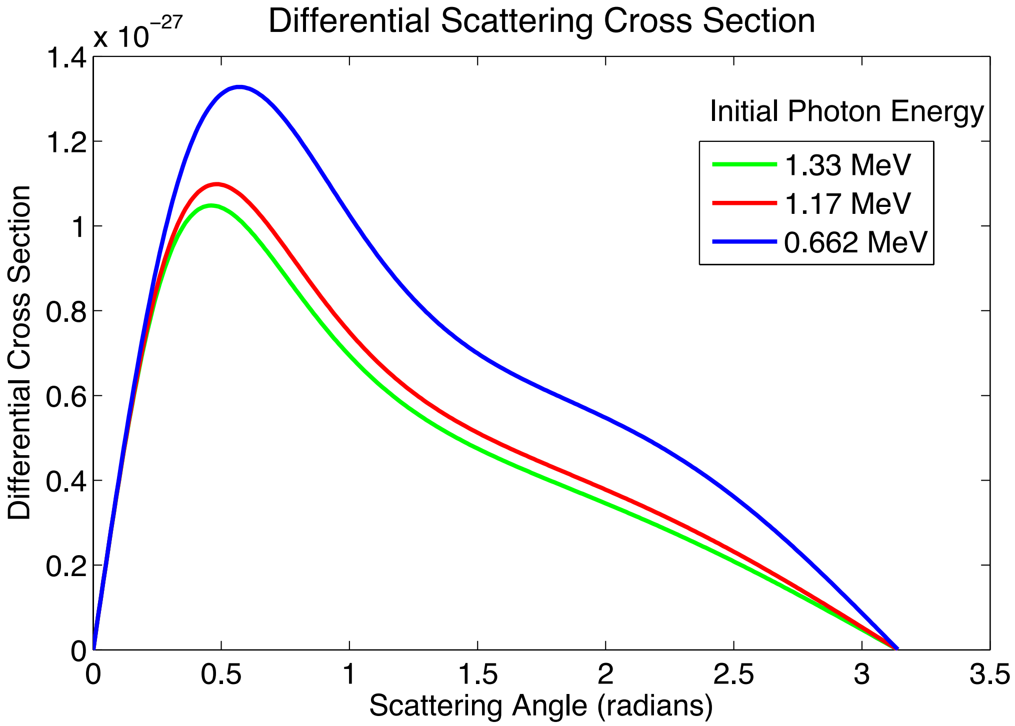

Figure 1.2 The differential cross section for Compton scattering as a function of the scattering angle θ for select initial photon energies

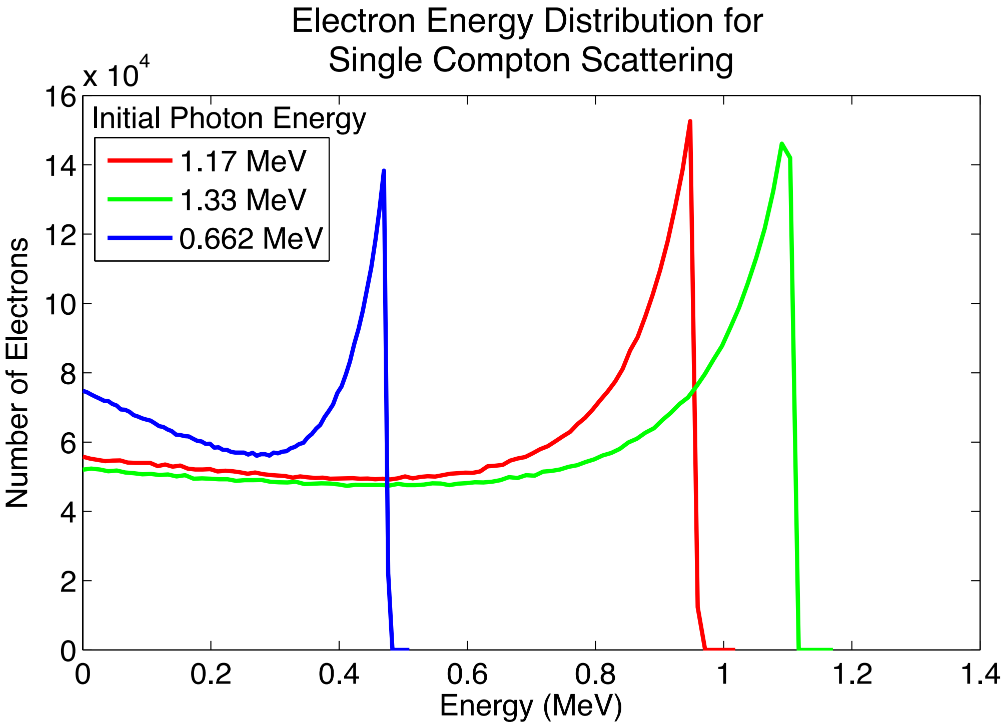

Figure 1.3 The electron energy distribution of single Compton scatters for select initial photon energies

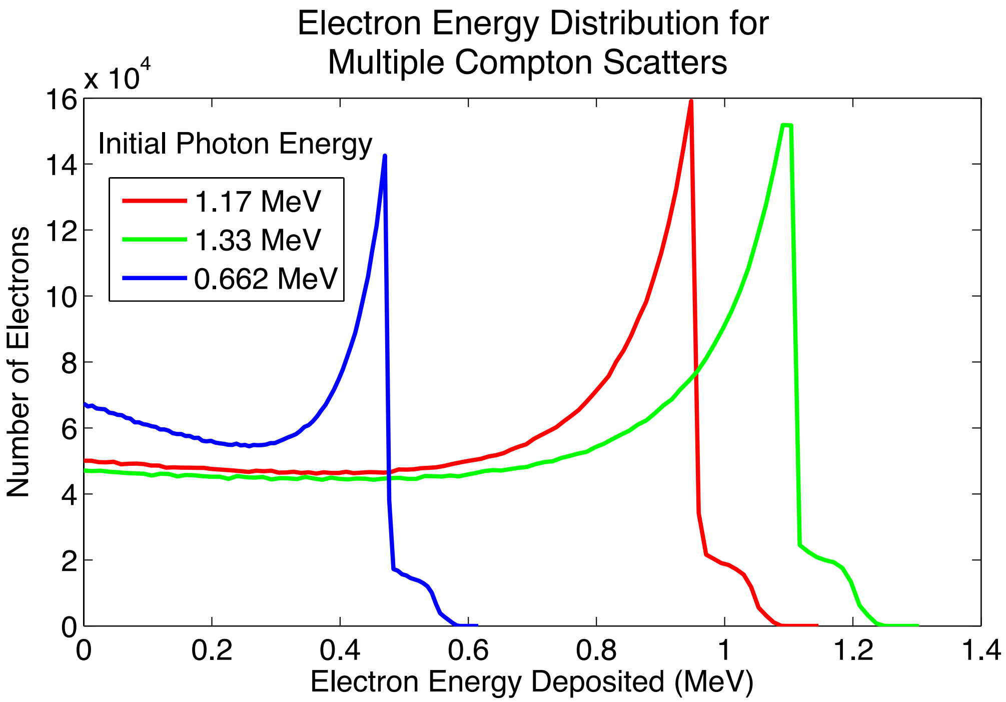

Figure 1.4 The electron energy distribution of multiple Compton scatters for select initial photon energies

scatters will simply broaden out the initial distribution. Using a simple model with a fixed probability of two or three scattering events gives a qualitative picture of what will happen in an actual detector (See Fig. 1.4).

Two separate processes exist where the gamma does impart all of its energy in a single reaction. The first is the photoelectric effect and the second is pair production. The photoelectric effect occurs only when a gamma ray interacts with an atom (not a free electron). The gamma ray is completely absorbed resulting in the ejection of one of the atom's bound electrons. Pair production occurs when the gamma ray is in the field of the atomic nucleus and is completely absorbed causing the emission of an electron-positron pair. This is only possible for gamma energies greater than twice the rest mass energy of an electron (1.02 MeV). For detectors employing typical organic scintillators the photoelectric absorption and pair production cross sections are negligible. Thus, for our detector, the Compton cross section dominates for all energies of interest. Photoelectric absorption is wholly negligible and pair production may contribute but only a very small fraction. This allows the sole use of the Compton electron energy distribution as a method for characterizing the detectors with gamma sources.

1.6 Photomultiplier Tubes

1.6.1 Theory

The PMT converts scintillator light to an electronic pulse via the photoelectric effect and an electron multiplication chain. The photocathode is coated with a material that has a sufficiently low work function to accomplish the conversion. The work function ϕ represents the smallest energy photon required to eject an electron from an atom in the material. Thus, the light output spectrum of the scintillator must be matched to the work function of the PMT. Subsequently, the kinetic energy of an ejected electron is:

$$\mathrm{E} = \mathrm{h}\nu - \phi \tag{1.17}$$

where h is Planck's constant, and ν is the frequency of the photon. The ejected electrons are accelerated to the first dynode of the PMT via a potential difference. Here they collide with and eject more electrons, which are then accelerated to the second dynode via a potential difference, and so on. This process continues until the end of the multiplication chain where the electrons are collected at the anode, thus creating a voltage that is proportional to the number of photons that strike the photocathode.

Despite this simple explanation, photomultiplier tubes are quite complex. Different models present different capabilities and limitations. The two main considerations with PMTs are efficiency and timing capability. Interestingly, the variables that affect these two considerations are closely connected and often the same.

In order to calculate the efficiency of the detector and the timing capabilities, we need to know what the ejected photoelectrons will do in the presence of the electric field caused by the first dynode and other focusing elements. To find the electric field inside of a PMT model we first have to calculate the voltage using Laplace's Equation:

$$\nabla^2 \mathrm{V} = 0 \tag{1.18}$$

Solving this analytically is possible for simple geometries, but developing a computational model that works for complex geometries proves to be much more useful. Consider the cartesian coordinate system for V, in which Laplace's Equation becomes:

$$\frac{\partial^2}{\partial x^2}\mathrm{V} + \frac{\partial^2}{\partial y^2}\mathrm{V} + \frac{\partial^2}{\partial z^2}\mathrm{V} = 0. \tag{1.19}$$

Now consider a grid where the x, y and z grid-points are evenly spaced by a distance h. By taking the centered finite difference approximation in cartesian coordinates, the second derivatives become:

$$\frac{\partial^2}{\partial x^2}\mathrm{V} = \frac{\mathrm{V}_{x+h,y,z} - 2\mathrm{V}_{x,y,z} + \mathrm{V}_{x-h,y,z}}{\mathrm{h}^2} \tag{1.20}$$

$$\frac{\partial^2}{\partial y^2}\mathrm{V} = \frac{\mathrm{V}_{x,y+h,z} - 2\mathrm{V}_{x,y,z} + \mathrm{V}_{x,y-h,z}}{\mathrm{h}^2} \tag{1.21}$$

$$\frac{\partial^2}{\partial z^2}\mathrm{V} = \frac{\mathrm{V}_{x,y,z+h} - 2\mathrm{V}_{x,y,z} + \mathrm{V}_{x,y,z-h}}{\mathrm{h}^2} \tag{1.22}$$

By substituting these back into Laplace's Equation and solving for V(x,y,z), we get:

$$\mathrm{V}_{x,y,z} = \frac{1}{6}\left[\mathrm{V}_{x+h,y,z} + \mathrm{V}_{x-h,y,z} + \mathrm{V}_{x,y+h,z} + \mathrm{V}_{x,y-h,z} + \mathrm{V}_{x,y,z+h} + \mathrm{V}_{x,y,z-h}\right] \tag{1.23}$$

Thus, the voltage at each point in space can be approximated by taking an average of its six cartesian neighbors. This equation can be used in an iterative method to find the solution with appropriate boundary conditions. We do not apply this to the boundaries because they do not obey Laplace's Equation, but they do affect the surrounding points in space that do obey Laplace's equation. Without the boundaries, we cannot solve for the interior points.

Implementing such an algorithm then gives the voltage contours inside the PMT's cathode-to-first-dynode region. Taking the negative gradient of this voltage function gives the electric field:

$$\vec{\mathrm{Efield}} = -\nabla \mathrm{V}. \tag{1.24}$$

Armed with the electric field, we can find the trajectory of any charged particle with any set of initial conditions within the PMT. Again, this is done computationally with some small time step $\Delta\mathrm{t}$, using the following equations:

$$\mathrm{v} = \sqrt{\frac{2\mathrm{E}}{\mathrm{m}}} \tag{1.25}$$

$$\mathrm{r} = \mathrm{r}_0 \tag{1.26}$$

$$\vec{F} = \mathrm{q}\vec{\mathrm{Efield}} = \frac{\mathrm{m}\Delta\vec{\mathrm{v}}}{\Delta\mathrm{t}} \tag{1.27}$$

$$\Delta\vec{\mathrm{v}} = \frac{\mathrm{q}}{\mathrm{m}}\vec{\mathrm{Efield}}\Delta\mathrm{t} \tag{1.28}$$

$$\vec{\mathrm{r}} = \vec{\mathrm{r}} + \vec{\mathrm{v}}\Delta\mathrm{t} \tag{1.29}$$

where E is the energy found from Eq. (1.17), and the initial direction is chosen randomly. Implementing this algorithm gives the desired information: where did the photoelectron's life end? Was it on the first dynode or some other part of the photocathode? If it was on the first dynode, how long did it take to get there? Only the electrons that reach the first dynode will actually produce a signal, and the difference in arrival times between the fastest and the slowest electrons affects timing capabilities.

1.6.2 A Quick Example

A simple model of a PMT gives a quasi-quantitative explanation of some important features. The variables we will consider in this model are: shape of the photocathode, and the shape and voltage of the first dynode. Consider a simple PMT that has a cylindrical photocathode with a small circular plate for a first dynode. The radius of the cylinder is 6.35 cm, its height is 7.62 cm, and it is held

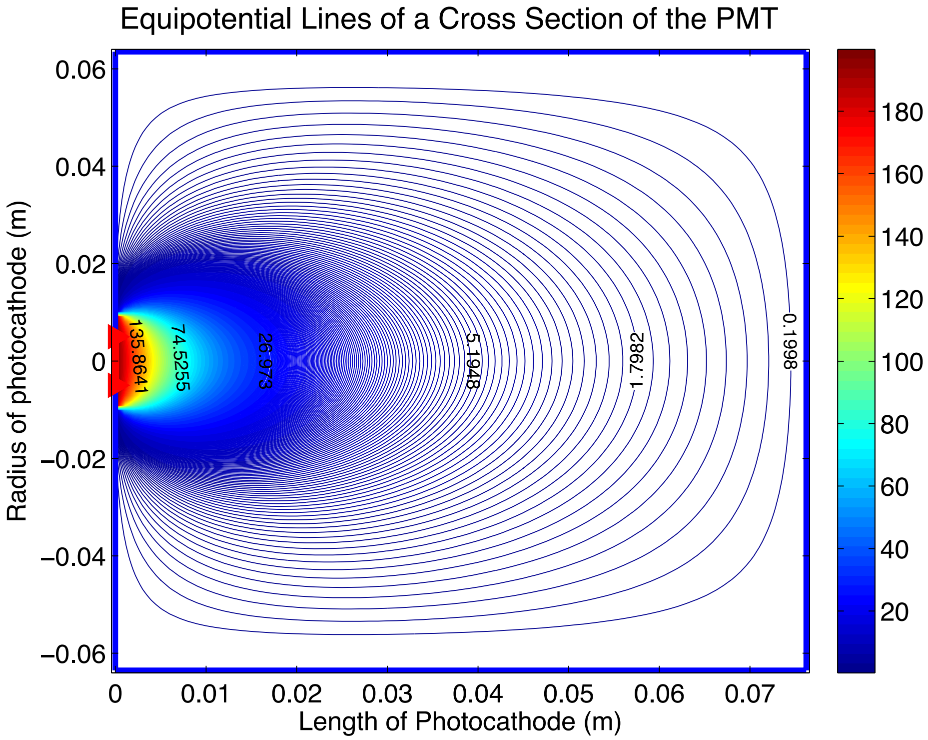

Figure 1.5 The equipotential lines for a cross section of the cylindrical PMT

at ground. The circular first dynode has a radius of 0.5 cm and is kept at a constant voltage of 200 volts at the base of the cylinder.

Finding the voltage using this algorithm provides equipotential surfaces. However, plotting the equipotential lines requires taking a cross section of the cylindrical photocathode; this is shown below in Fig. 1.5, where the blue indicates the boundary of the photocathode and the red indicates the first dynode. As you can see from the figure, the voltage drops off rapidly as the distance from the first dynode increases.

The electric field is much harder to see considering the very small values at most of the interior points. However, the electric field and the initial kinetic energy of the electrons are the values that actually give the timing and efficiency of the PMT. We do this by randomly choosing a radius for a given photoelectron. Then we choose its initial direction by randomly distributing the initial momentum along the 3 cartesian coordinates. Then Eq. 26 through 31 give the trajectory of the electrons.

The calculated efficiency of the PMT requires a simple stipulation. If the electron enters a boundary (blue) then it doesn't contribute to the pulse, and we say it is "bad". If the electron enters the first dynode (red) then we count it as a "good" photoelectron. The ratio of good electrons to the total number calculated gives the overall efficiency of the PMT. In our case, the number of good electrons was 4,568 out of a 22,000 photoelectron run, giving a total efficiency of 20.76%. We can also calculate the efficiency of the PMT as a function of radius, which is important to keep in mind depending on the geometry of the detector (see Fig. 1.6). It is evident that the efficiency at the edges is a fraction of what it is at the center. This is caused by a larger part of the solid angle being taken up by the photocathode around the edges. This will be the case in almost any PMT due to these edge effects.

The timing is also simple to calculate. For each photoelectron the time of flight to the first dynode is found by multiplying the number of iterations required by the time step Δt. If Δt is sufficiently small, the errors in this calculation will be negligible. So now we have a time of flight associated with each photoelectron. This makes mocking up a PMT pulse relatively effortless: simply make a histogram of the array of times of flight, choosing some sampling rate. This is shown in Fig. 1.7 for the cylindrical PMT example with a sampling rate of 4ns.

The timing capabilities of the detector in question will not be explored in this paper. Therefore, an in-depth discussion of the effects of the PMT on these qualities is beyond the scope of this paper. However, it is important to note that this theoretical model does provide great insight into this important aspect of the detector system.

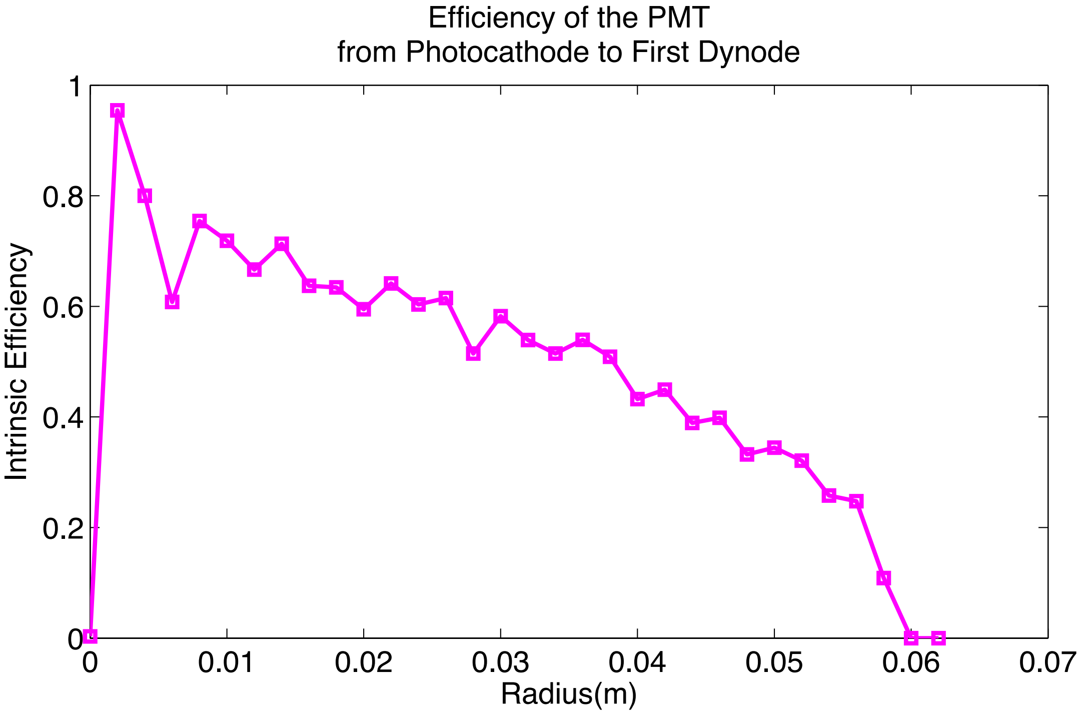

Figure 1.6 The intrinsic efficiency of the photocathode to first dynode process as a function of radius

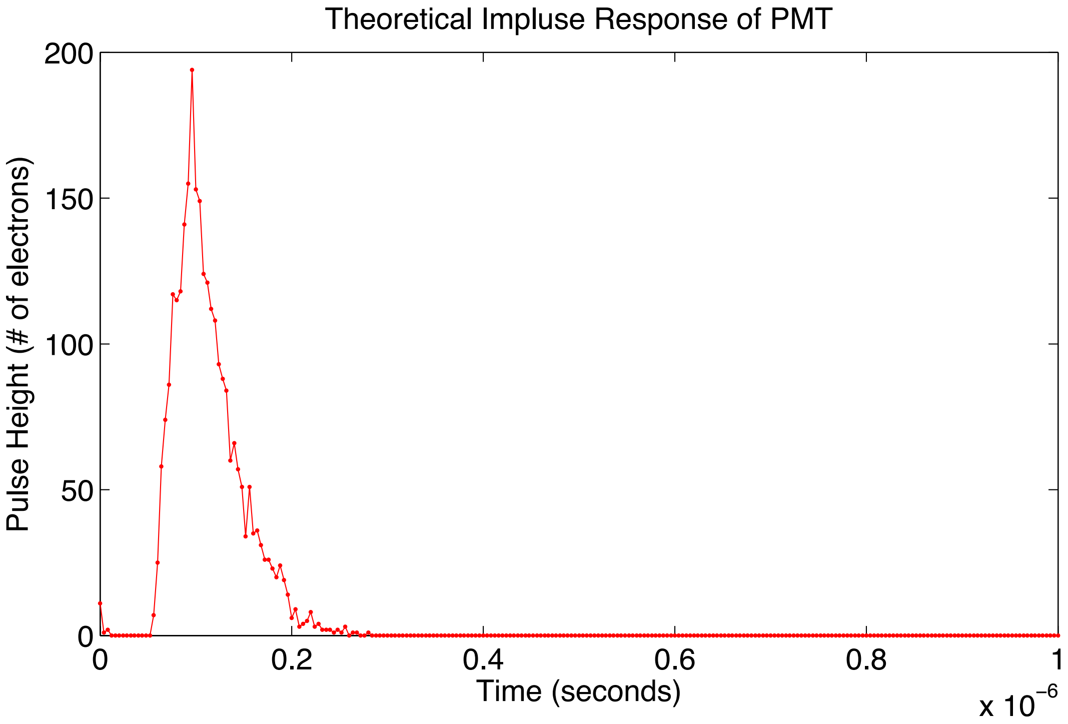

Figure 1.7 A theoretical impulse response of a uniformly illuminated PMT with a sampling rate of 4ns

Chapter 2

Detector Design

We present here an argument for the chosen design of the detector, including the capture material and geometry employed. A number of capture materials exist with varying thermal neutron capture cross sections. The type of capture material used determines what geometry and scintillation method to employ. The detector in question exploits neutron-gamma reactions. For this type of reaction, several capture materials exist: cadmium, gadolinium, samarium, and europium.

Our detector utilizes 0.1mm cadmium foils inserted between 1cm thick slabs of plastic scintillator (replaceable by liquid scintillator). A reflective material, such as aluminized polyester, surrounds the cadmium foils, as well as the whole detector volume. These plastic slabs create a detector volume in the shape of a cylinder which is optically coupled to a 5-inch circular PMT. This produces a detector volume of 1544cm^3. The detector is 15% by weight cadmium, despite the cadmium taking up a negligible amount of volume $(\sim 1\%)$. The details of the geometry were chosen by computer modeling of the detector.

2.1 An Introduction to Monte Carlo for Neutral Particles

Much of the detector design occurred without building a detector. This was accomplished with the aid of a computer algorithm called Monte Carlo for Neutral Particles (MCNP), produced, updated and maintained by Los Alamos National Laboratory (LANL) [4]. This code achieves this by modeling neutron paths and interactions through the detector. The user is required to input the geometry of the problem and the chemical makeup of each zone of geometry. One can also define a radioactive source inside this geometric model. This allows the user to construct a theoretical model of a detector and compute its response to different radioactive sources.

MCNP follows a neutral particle from its creation in the radioactive source through each zone of the geometry. At each point the code calculates the probability of that particle interacting with its environment in each possible way, whether it be simple scattering, capture, etc. Because of the probabilistic nature of these interactions, the code figuratively "rolls the dice" to see if a particle interaction will occur or not (hence the casino-like name of Monte Carlo). The code follows this neutral particle through until its end, while keeping track of the important information concerning its several interactions. Of course, this process is not accurate for small numbers of particles, but as we let the code follow larger and larger numbers of neutrons, the error in the results decreases.

This powerful algorithm allows us to model and evaluate different detector materials and geometries without building them. Much of our design process took place inside this algorithm. This chapter of the paper focuses on our pre-production synthesis and analysis of the MCNP code that helped us design a prototype detector.

2.2 Computaional Methods

The geometry and materials used in the capture-gated method affect a number of qualities. The qualities of concern are capture efficiency, mean capture time and optical viability. The geometry of the detector influences both the optics and the capture efficiency of the detector, and so they had to be considered in tandem.

The first geometrical consideration is the method of integrating the capture material with the scintillator. A number of methods exist that achieve this. One such method involves a heterogeneous mixture of crystals that include the capture material and the polymer in the scintillator. We modeled this type of setup using small spheres of GdF_3 and CdF_3 distributed inside a cylindrical detector.

A series of MCNP runs after this initial run led us to a model that incorporates the capture material independently of the scintillator. The capture material does not have to scintillate, nor does it have to be optically coupled in any way to the scintillator. This led to a geometry where scintillator slabs alternate with metal foils of capture material. We modeled detectors using both gadolinium and cadmium foils to determine which material had higher capture efficiency. After this we optimized the foil and scintillator thickness.

In each stage, a bare (un-shielded) ^{252}Cf source was employed. ^{252}Cf has a spectrum similar to plutonium and other fission neutron sources, but it is also available commercially. This makes it ideal for use in theoretical models because it allows us to compare experimental results with the results we received from MCNP (see Sec. 3.2-3). We calculated the capture efficiency as the number of neutrons captured divided by the number of neutrons incident on the face of the detector.

2.3 Results

Shown in Table 2.1 are the data collected from a series of MCNP runs that show various theoretical gadolinium and cadmium crystals interspersed inside a detector volume in the shape of 1.175mm spheres.

The next set of MCNP runs shows the efficiency of metal foils .25mm thick separated by zones

Chemical Form	Capture Material	Atomic Fraction(%)	Capture Efficiency(%)	Scintillator
CdF_3	^{113}Cd	0.859	10.45	PVT
GdF_3	^{157}Gd	0.640	11.88	PVT

Table 2.1 Cadmium and gadolinium flouride crystal spheres (radius 1.175mm) interspersed in PVT

Chemical Form	Capture Material	Atomic Fraction(%)	Capture Efficiency(%)	Scintillator
Cadmium Metal	^{113}Cd	1.215	18.35	BC 517H
Gadolinium Metal	^{157}Gd	0.795	19.82	BC 517H

Table 2.2 Cadmium and gadolinium metal foils (.25mm thick) seperated by .898cm thick plastic scintillator

of scintillator .898cm thick (see Table 2.2). The total detector volume encompassed a cylinder 4 inches thick and 5 inches in diameter.

Displayed in Table 2.3 are data that display the results of a series of MCNP runs that vary the thickness of the cadmium foils. The only added element in this run is that the cylinder detector volume has been wrapped in cadmium foil, known below as the can. The efficiency of the foils and the can are shown separately in columns 2 and 3 respectively.

Cadmium Thickness (mm)	Foil Efficiency(%)	Can Efficiency(%)	Total Efficiency(%)	Scintillator
0.10mm	11.26	1.84	13.10	PVT
0.25mm	11.49	1.53	13.02	PVT
0.50mm	11.45	1.32	12.78	PVT
1.00mm	11.08	1.05	12.13	PVT

Table 2.3 Capture efficiency in different zones of the detector as a function of cadmium-foil thickness

Efficiencies in percent with:	0.1mm Cadmium Foil	0.2mm Cadmium Foil	# of Cadmium Sheets
0.5cm scintillator	21.64	21.71	24
1.0cm scintillator	20.37	20.36	12
1.5cm scintillator	18.2	-	8
2.0cm scintillator	16.2	-	6

Table 2.4 Capture efficiency of cadmium foils with varying scintillator thickness and number

Shown in Table 2.4 are results obtained that incorporate both cadmium thickness and scintillator thickness. The detector in this analysis is a cylinder 6 inches tall and 5 inches in diameter. Note that the scintillator used in this run differs from the pervious runs, and therefore the discrepancy between capture efficiency for correlated thicknesses.

2.4 Design Conclusions

The first notable result is the difference in capture efficiency between the "crystals" and the metal foils. The metal foils have almost twice as much capture efficiency. Using pure metal allows for more of the capture material to be inserted into the system relative to the amount of scintillator without adding too much non-scintillating mass. This is important because of the dependence of the detector on Compton-scattered electrons for the capture pulse. It is ideal to have the smallest volume of capture material into the system as possible while still obtaining a realistic capture efficiency. Adding too much capture material will greatly increase the amount of gamma energy lost in non-scintillating material, thus degrading the capture pulse height.

The thermal neutron capture cross section for gadolinium is 259,000 barns, more than 10 times higher than the 20,000 barns for cadmium. Despite this, the capture efficiency of the cadmium foils shown in Table 2 is only 7.4% smaller than the gadolinium foils and still presents a realistically efficient detector. This lower efficiency is acceptable considering the cost differences between cadmium and gadolinium. These results prompted the choice of cadmium over gadolinium in our design.

Once the field was narrowed down to cadmium metal foils, the question of metal thickness and plastic thickness ensued. Tables 3 and 4 show evidence that the optimum thickness for the cadmium foils is 0.1mm, and the optimum thickness for the scintillator is 1cm. Table 4 suggests that an increase in cadmium foil thickness from 0.1mm to 0.2mm has a negligible effect on the capture efficiency. Due to the bad optical quality of cadmium or gadolinium foils, a reflective coating must be used at the interface between the scintillator and the capture material. This reflective coating will still cause some absorption of scintillated light. Due to the thin slab nature of the scintillator, the number of reflections can be large, causing a large amount of absorption for light emitted in the end of the detector far from the PMT. The amount of absorption depends on the thickness of these slabs. The 0.5cm scintillator does produce about a 1% increase in capture efficiency; however, when considering the amount of reflection thinner slabs would create for the scintillated light, the 1cm scintillator stands out as the best option. All of these results culminated in a detector design described in the introduction to this section.

Chapter 3

Detector Characterization

3.1 Characterization Introduction

The unique pattern of slabs along with the introduction of non-scintillating metal capture material introduces changes to an ideal plastic detector volume. These changes affect the characteristics of the detector. This chapter introduces the methods employed to measure these changes quantitatively, the results of these measurements, and a discussion of the results. An analysis of the capability of the system to detect neutrons will follow in chapter 4.

We divided these changes into three stages: pure plastic; plastic and reflective aluminized polyester, and plastic; aluminized polyester and cadmium. To measure the changes caused by deviations from the ideal pure plastic detector we utilized a mono-energetic and quasi monoenergetic gamma source. The theory explained in Sec. 1.5 provides a framework for characterizing the detector using gamma sources. The Compton edge, or distribution of electron energies deposited in the detector, provides a benchmark for each stage of the detector. The area of a given pulse is proportional to the energy deposited; thus, plotting the pulse area distribution gives the electron energy distribution from Compton scattering, different only by a multiplicative factor.

Because of intrinsic broadening caused by a number of factors, the energy at the peak of the distribution is not traditionally used. Instead, "half-way down the Compton edge" is used as the calibrating value. This is simply the energy value where the number in the distribution is equal to half the number in the peak channel. This is best illustrated in Fig. 3.1, as seen below. Finding this value at each stage of the experiment provides a quantitative method for describing the changes in light output at each stage.

We employed a ^{137}Cs and ^{60}Co source at each stage. The source was placed 44 ± 0.5 cm away from the face of the detector. This distance was chosen so that pileup from the source did not occur in the detector while still producing reasonable rates. The detector was placed in a light-tight can for each experiment; the PMT was powered with a high voltage power supply running at 1.2 kV. The output of the PMT connected to one channel of a 4-channel digitizer (Caen model DT5720). The sampling rate of the digitizer is 250 MHz, with 12-bit resolution on the range of -1 V to 1 V. The acquisition window was 1,024 samples long (4 μs) with a trigger threshold of 10mV. Every run includes 100,000 pulses of data. The set-up was completely reproducible at each stage of the experiment.

3.2 Results

The overlay of the pure plastic runs for both ^{60}Co and ^{137}Cs is shown below in Fig. 3.2.

The results for the three ^{60}Co stages are shown below in Fig. 3.3 and Table 3.1. The figure displays the pulse area distribution for each run while the table displays the values for the peak and halfway down the Compton edge.

The results for the three ^{137}Cs stages are shown below in Fig. 3.4 and Table 3.2, with the figure and table displaying the same data as for the ^{60}Co.

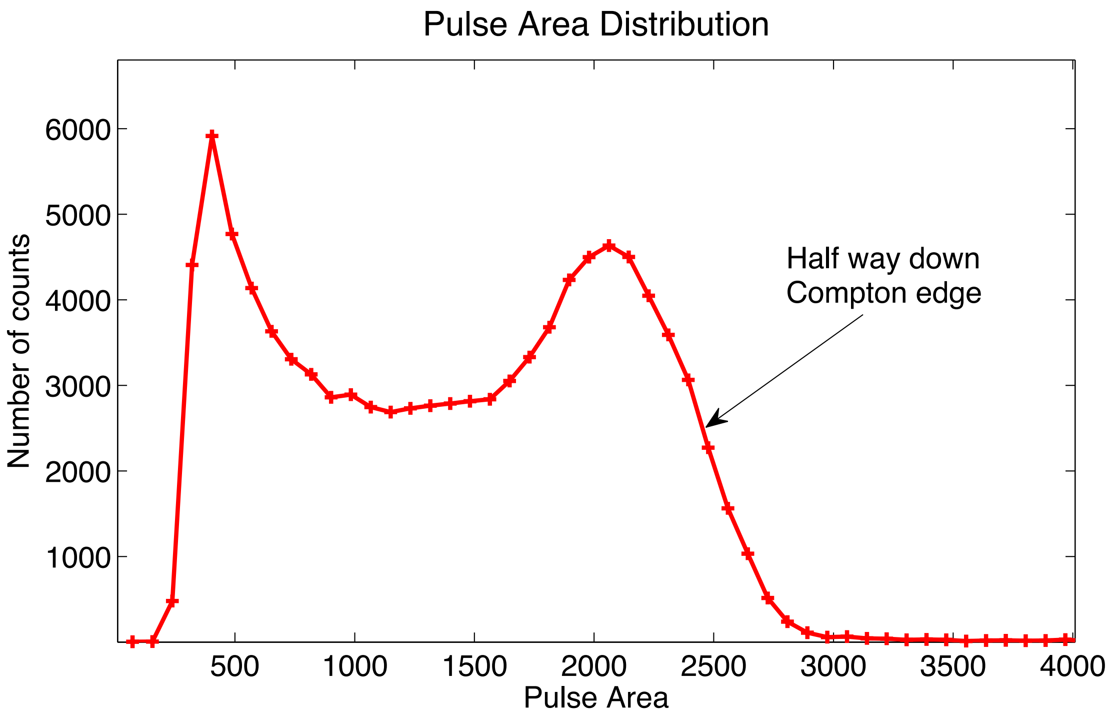

Figure 3.1 Illustration of the method of defining electron energy equivalents from Compton scattering by using half-way down the Compton edge

^{60}Co Stages	Peak Value (channels)	Half-way Value (channels)
Pure Plastic	2062	2472
+Aluminized Polyester	1865	2322
+Cadmium and Aluminized Polyester	1598	1964

Table 3.1 Results displayed for three characterization runs employing ^{60}Co

^{137}Cs Stages	Peak Value (channels)	Half-way Value (channels)
Pure Plastic	1049	1214
+Aluminized Polyester	831	1041
+Cadmium and Aluminized Polyester	525	703

Table 3.2 Results displayed for three characterization runs employing ^{137}Cs

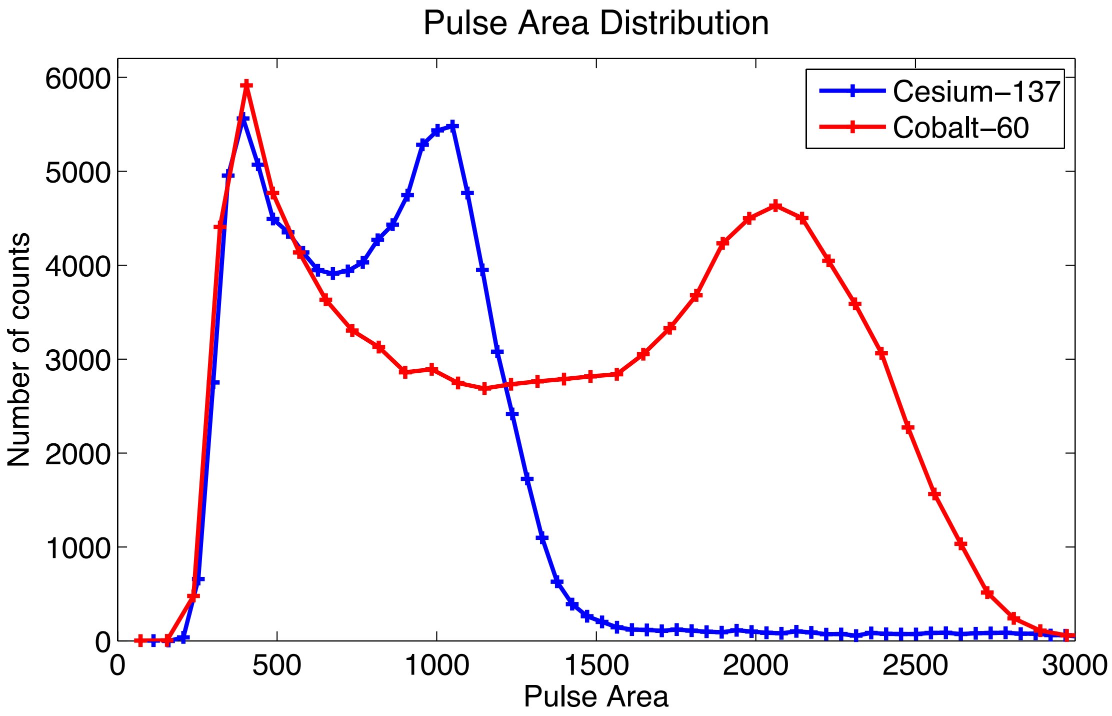

Figure 3.2 Pulse area distributions in pure plastic for both ^{60}Co and ^{137}Cs

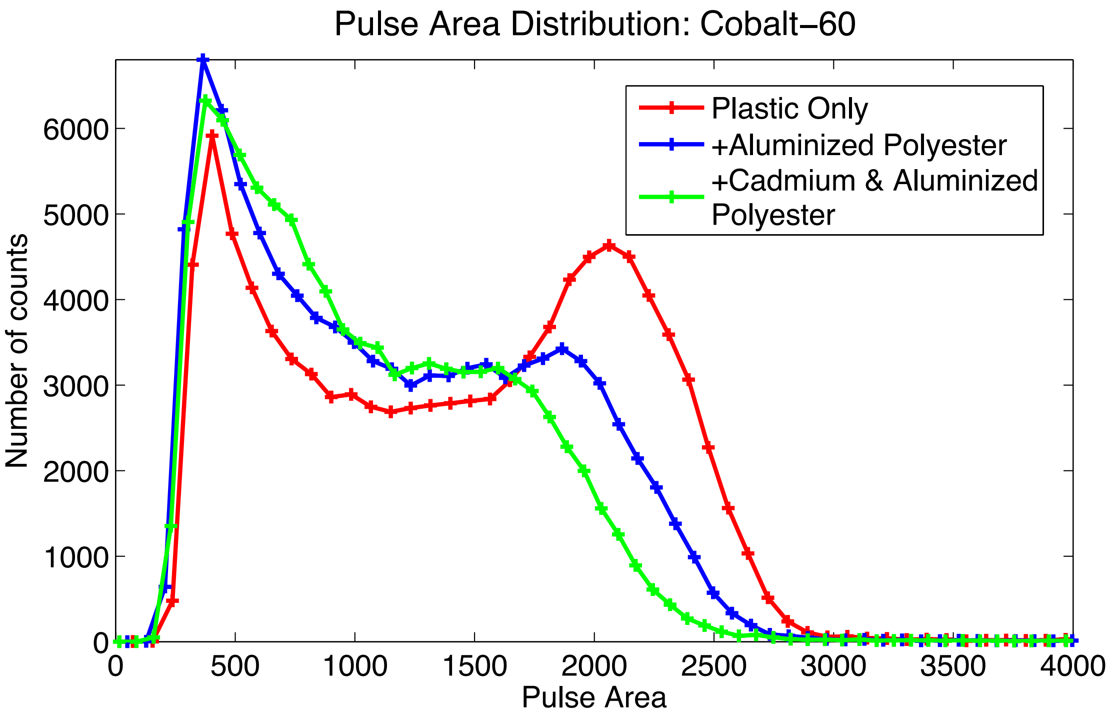

Figure 3.3 The pulse area distributions from ^{60}Co for all three detector stages

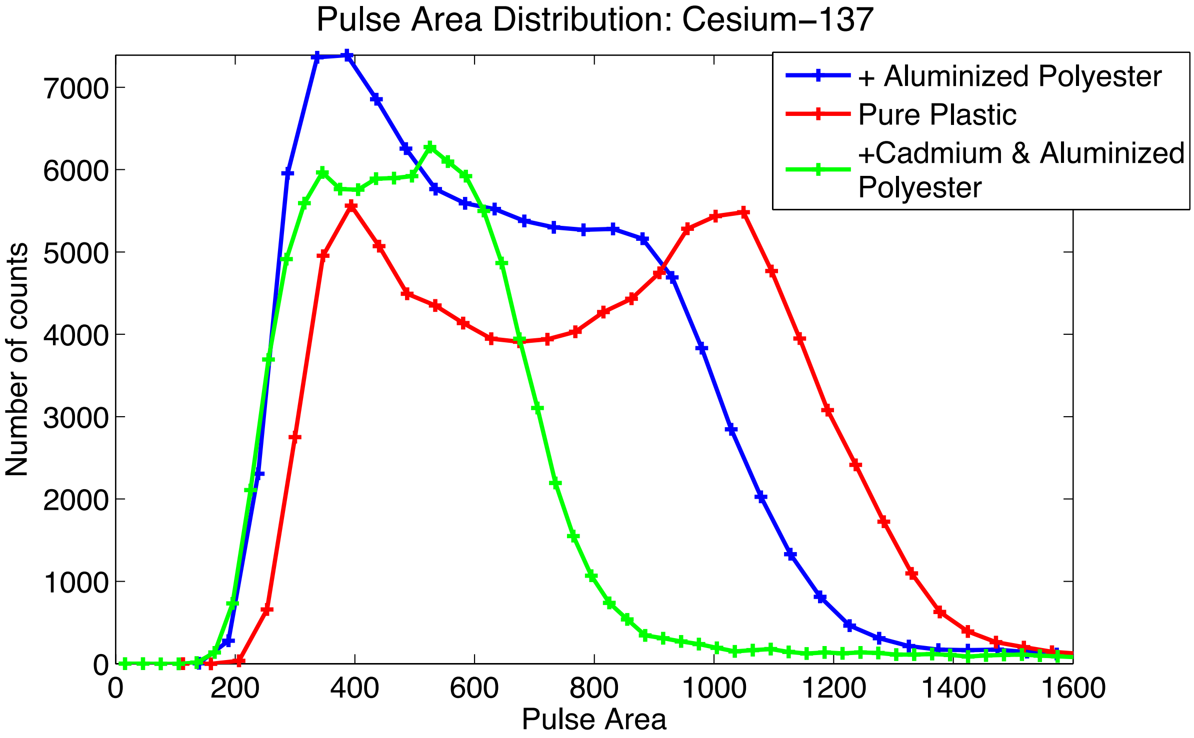

Figure 3.4 The pulse area distributions from ^{137}Cs for all three detector stages

3.3 Analysis and Discussion

It is important to note how well Fig. 3.2 agrees with theory, as explained in Sec. 1.5. The distribution described by the Klein-Nishina formula is seen in both the cobalt and cesium distributions. Of course, broadening is present as the system is not perfect. It is also important to note that the ratio of energy deposited by the cesium to that of the cobalt agrees also with theory. The energy of the cesium gamma ray is 0.662 MeV, giving it maximum electron energy of 0.478 MeV according to Eq. 1.16. The cobalt source gives off two simultaneous gammas with energies of 1.17 and 1.33 MeV, with maximum electron energies of 0.960 and 1.12 MeV respectively. The average of these two values is 1.04 MeV. This gives a ratio of cesium electron energies over average cobalt electron energies as 0.46. The ratio of half way down the Compton peak values, from Tables 3.1 and 3.2, is 0.49.

All three cobalt runs, displayed in Table 3.1 and Fig. 3.3, have some interesting features. First of all, the peak in the distribution is very apparent in its ideal pure plastic form; however, when we add reflective layers in between the slabs, the peak in the distribution disappears. We propose that a number of variables cause this. First of all, by introducing the slab geometry, we confine the light to move in discrete zones. Each event may produce light in only some of these zones, sampling only a portion of the photocathode. Due to the irregular response of the photocathode, as explained in Sec. 1.6, this means that events that create the same amount of light in the scintillator may have very different pulse areas in the end. This same effect can also be seen in the cesium data.

With the insertion of reflective material there is an overall drop in pulse area. This drop of 6.2% for cobalt and 14.3% for cesium is due to photon absorption. If the reflector had a reflectance of 1, then there would be no theoretical change. However, the material is not a perfect reflector, and so photon absorption occurs in proportion to the number of reflections that take place. This causes the general degradation of pulse height and thus pulse area seen in each of the distributions. The added non-scintillating polyester and aluminum also causes a loss in energy because scattered electrons will deposit some of their energy here.

The same effect causes the further reduction of pulse area, or loss of electron energy, as cadmium is added in between the plastic slabs and the aluminized polyester. Electrons simply lose energy inside the metal, which does not convert the electron energy to light. This effect is proportional the ratio of the non-scintillating mass added to the scintillator and the scintillator mass. The detector is 15% by weight cadmium, and so we would expect a 15% drop in pulse area between the run with reflective material and the run with cadmium. For the cobalt run, the drop in pulse area as measured by halfway down the Compton edge is 15.4%. For the cesium run, the same calculation yields 32.5%.

Why do the cesium runs report such a greater loss than the cadmium runs? The answer lies in the non-linear energy loss per unit length of electrons in the metal. At lower energies the electrons lose much more energy per unit length than electrons at higher energies [5]. This causes the larger drops in the cesium distributions between stages.

In conclusion, the detector's response to various deviations from an ideal pure-plastic volume were characterized. These changes were predicted and are explained theoretically. Most importantly, the changes introduced at every stage do not destroy the detector's viability. The system has proven to be able to detect charged particles with light output less than 0.477 MeVee (MeV electron equivalent). The implications of these conclusions will be discussed in depth in the next chapter.

Chapter 4

Neutron Detection Capabilities

4.1 Introduction

First, we want to measure the absolute efficiency of the detector. The response of the detector to neutrons is spectrally dependent. Because the detector in question is being proposed mainly for applications in national security, the ^{252}Cf spontaneous fission spectrum is the most useful and most available. In short, we want to measure the fraction of ^{252}Cf neutrons incident on the face of the detector that produce a measurable start pulse, capture in the cadmium, and then produce a measurable stop pulse thus producing a dual pulse signature (DPS). This produces formulas for DPS rates, intrinsic efficiency, and absolute efficiency given by:

$$\mathrm{R}_{doubles} = \mathrm{R}_{source}\frac{\Omega}{4\pi}\mathrm{F}_T\mathrm{F}_C\mathrm{E}_\gamma \tag{4.1}$$

$$\mathrm{E}_{intrinsic} = \mathrm{F}_T\mathrm{F}_C\mathrm{E}_\gamma \tag{4.2}$$

$$\mathrm{E}_{absolute} = \frac{\Omega}{4\pi}\mathrm{F}_T\mathrm{F}_C\mathrm{E}_\gamma \tag{4.3}$$

where R_{source} is the rate of neutrons emitted from the source, Ω is the solid angle, F_T is the fraction of neutrons that give a start pulse above threshold, F_C is the fraction that produce a start pulse and also that capture in the cadmium, and E_γ is the efficiency for detecting the gamma rays emitted as a result of neutron capture in cadmium. Intrinsic efficiency only takes into account the neutrons that hit the front face of the detector, while absolute efficiency takes into account all of the neutrons emitted by the source. I will focus on intrinsic efficiency, noting that absolute efficiency is merely a factor of $\frac{\Omega}{4\pi}$ different. The major unknown in this equation, that unfortunately is not measurable experimentally or easily calculated theoretically, is E_γ. This is unknown as the spectrum of cadmium-capture gammas released in this reaction is unknown. However, we can calculate the product of the three, which is the intrinsic efficiency. Using MCNP, we also obtain F_T and F_C which gives us E_γ by deduction.

The ideal detection system includes the introduction of a second neutron-insensitive detector for the purpose of doing an accurate accidental subtraction. This detector is built to the same specifications as the cadmium detector except that a non-neutron-capturing metal of similar properties replaces the cadmium. The goal is to find a metal that produces the same distribution of electron energies from Compton scattering and from proton-recoil pulses in the plastic. So far, tin has proved to be the frontrunner in this endeavor, despite the continued search for the best metal. The use of this alternate provides two identical detectors in response to gamma rays, but two very different detectors in response to neutrons.

For the purpose of measuring efficiency, there are two types of background DPS that can occur in the cadmium detector. First, there are cosmic ray neutrons, and second, there are background of gamma rays. Both such signatures do not come from the ^{252}Cf source and therefore must be subtracted off. This is relatively easy to do: simply run the cadmium detector with no source present, producing a rate of DPS of background. This rate can easily be subtracted from the ^{252}Cf foreground measurement. The second type of accidental DPS prove more troubling. These DPS come from the gamma rays given off from spontaneous fission. These cannot be accounted for in a background run because they only originate in the fission source.

That is where the neutron-insensitive detector provides a measure of the accidental rate from non-neutron particles. Using the ^{252}Cf source, the alternate detector will give primary and secondary pulses from neutrons and gamma rays from ^{252}Cf SF, but it will not provide secondary pulses from neutron capture in cadmium. Thus, a subtraction of the number of DPS in the alternate detector from the cadmium detector yields the desired result. The following equations summarize this explanation symbolically:

$$\mathrm{Doubles}_{Cd} = \mathrm{Doubles}_{CdForeground} - \mathrm{Doubles}_{CdBackground} \tag{4.4}$$

$$\mathrm{Doubles}_{Alternate} = \mathrm{Doubles}_{AlternateForeground} - \mathrm{Doubles}_{AlternateBackground} \tag{4.5}$$

$$\mathrm{TotNeutrons} = \mathrm{Doubles}_{Cd} - \mathrm{Doubles}_{Alternate} \tag{4.6}$$

$$\mathrm{E}_{intrinsic} = \frac{\mathrm{TotNeutrons}}{\mathrm{R}_{source}\frac{\Omega}{4\pi}\mathrm{t}} \tag{4.7}$$

where t is the length of time of the run.

The comparison of two separate detectors both employing different PMTs requires careful calibration in order to match the gain. This can be done either by matching the voltage delivered to the PMT or by adjusting a hardware or software threshold.

Unfortunately, we have not been able to identify a metal that has a spectral response similar enough to that of cadmium. Shown in Fig. 4.1 is the electron energy distribution for the detector with cadmium and tin. This is actually the same physical detector and PMT with the metal being the only difference.

Despite these differences, the viability of the subtraction method can still be illustrated with the alternate detector employing tin. Instead of analyzing the data quantitatively by using the equations given above, we can understand the method qualitatively by understanding the physical principles involved. The main quantity that allows us to differentiate the accidental DPS from the neutrons is the time between the start and stop pulse. Accidental double pulses will produce a "capture" time

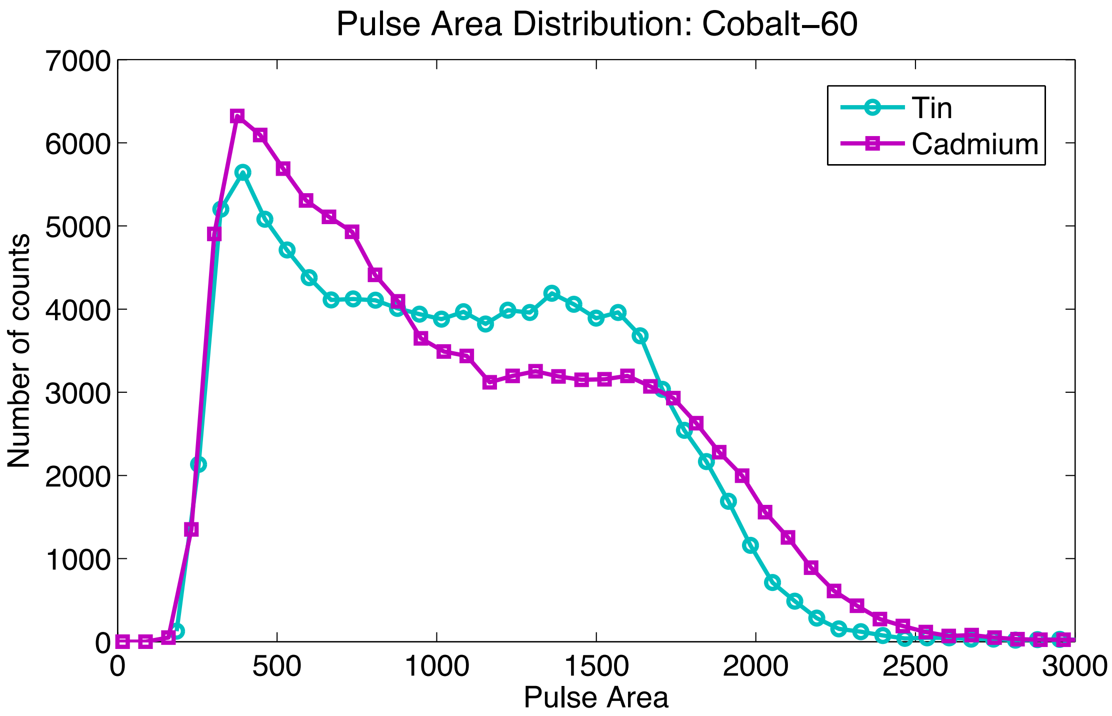

Figure 4.1 Difference in pulse area distributions arising from ^{60}Co in Cd and Sn detectors

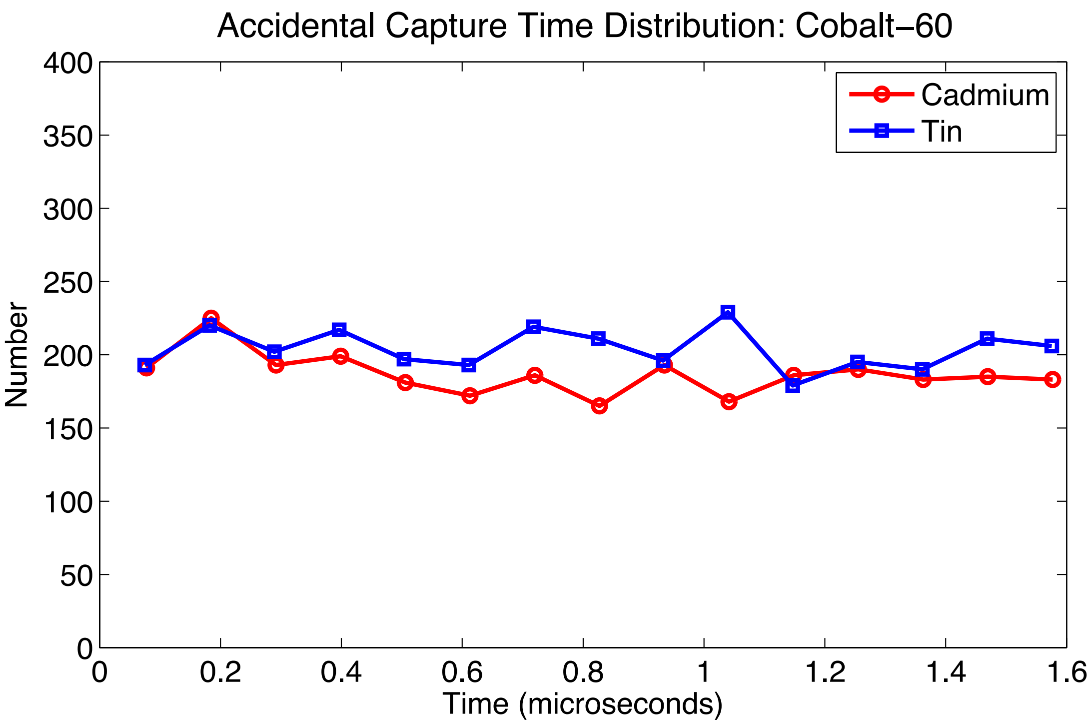

Figure 4.2 Little difference in capture time distributions (time between start and stop pulse) arising from ^{60}Co in the Cd and Sn detectors

distribution that is flat. This means that for a reasonably sized time window (on the order of 50μs), there is equal probability that the second pulse will occur anytime after the first pulse within the window. This is not the case for neutron capture. Depending on the spectrum of neutrons, the neutron will take a certain amount of time to moderate to sufficiently low energy for capture. This means that the first and second pulse have some correlation in time. The results are seen in Figs. 4.2 and 4.3.

The first of these shows an accidental capture time distribution for both cadmium and tin using ^{60}Co. As expected, the two distributions are flat and essentially identical. However, when a ^{252}Cf source is introduced, the distribution changes quite noticeably, as seen in the second figure. The area between the two distributions in the second figure is the same quantity described by Eqs.

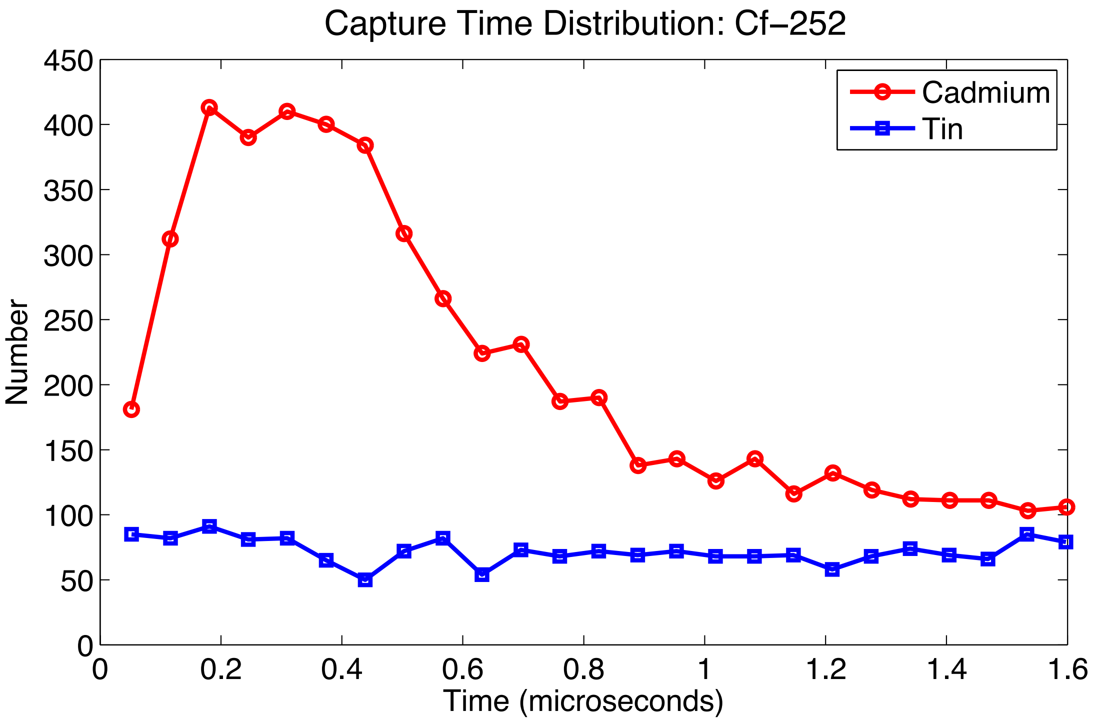

Figure 4.3 Large difference in capture time distributions (time between start and stop pulse) arising from ^{252}Cf in the Cd and Sn detectors

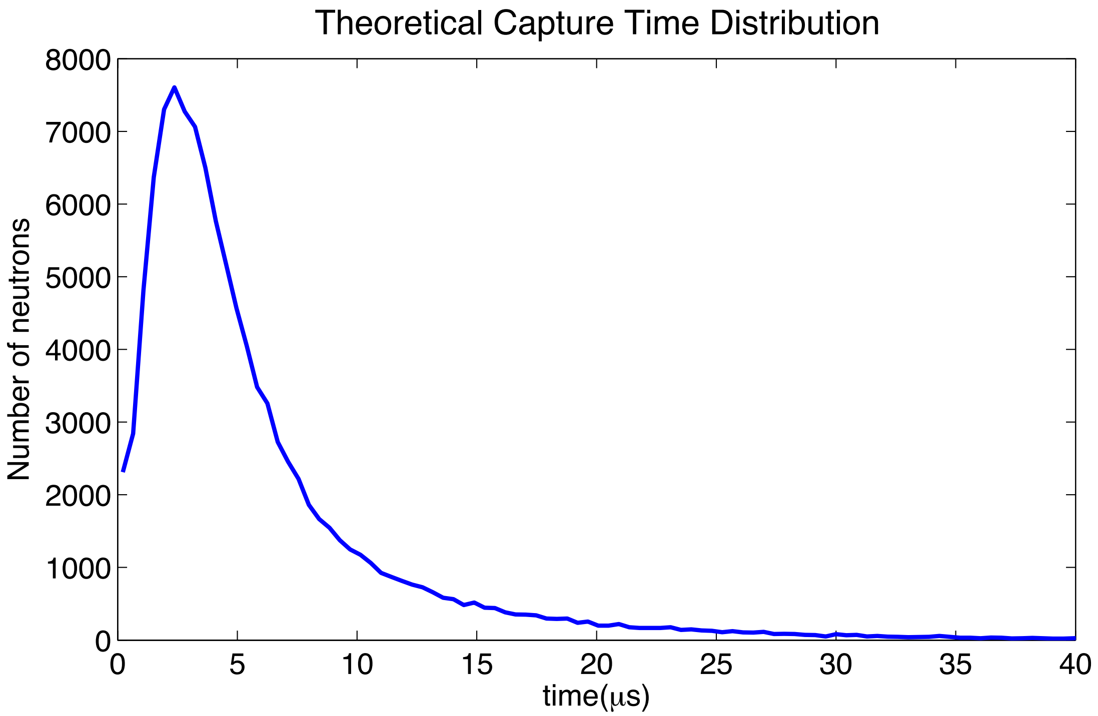

Figure 4.4 Theoretical capture time distribution from ^{252}Cf in the Cd detector

4.1-4.3, as the total number of neutrons detected. It is apparent that this method is viable, and if a suitable metal alternate can be found it would prove useful in measuring the efficiency of the detector and even more useful in national security applications.

For the purpose of measuring the absolute efficiency of the detector we employed a somewhat inferior method. This method utilizes the fact that the probability of getting a second pulse that resulted from neutron capture in cadmium goes asymptotically to zero as the time between the pulses approaches infinity. In practice, the probability is negligible at $\sim 25-32\mu$s. This is shown theoretically using MCNP (see Fig. 4.4). At times after this the majority of dual pulses are accidentals caused by the source, the same measurement given by the alternate detector. Of course, it is inferior because it is impossible to know with certainty how many neutrons are capturing at these times, but if the time window is long enough the errors become negligible.

This method requires taking an average of these accidental double rates for each bin in the distribution where negligible amounts of neutron capture still happen. Consider a distribution binned with equal bin widths $\Delta\tau$ and with N number of bins. There are η number of bins for which there are negligible amounts of neutron capture, each with a number of dual pulse signatures δ_i. This gives the following equations for finding the intrinsic efficiency:

$$\mathrm{AccidentalDoubles} = \mathrm{N}\frac{\sum_i \delta_i}{\eta} \tag{4.8}$$

$$\mathrm{TotNeutrons} = \mathrm{Doubles}_{Cd} - \mathrm{AccidentalDoubles} \tag{4.9}$$

$$\mathrm{E}_{intrinsic} = \frac{\mathrm{TotNeutrons}}{\mathrm{R}_{source}\frac{\Omega}{4\pi}\mathrm{t}} \tag{4.10}$$

where $\mathrm{Doubles}_{Cd}$ still includes the subtraction of background, as above. This method will be employed in the following sections to calculate the intrinsic and absolute efficiency.

4.2 Experimental Setup

Because of the need to know the spectrum, a major cause for concern is room return. This occurs when neutrons from the source scatter off of materials in the room, lose energy, and then enter the detector. This smears out the energy spectrum and artificially increases the efficiency. We overcame this obstacle by hoisting the detector in the middle of BYU's Indoor Practice Facility (IPF), which is an enclosed football field. We were able to place the detector 50 feet into the air, halfway between the floor and ceiling, and about 75 feet from two walls and further still from the other two. This realistically reduced the fraction of room-return neutrons to a negligible amount.

The signal from the detector was routed again to a Caen DT5720 Waveform Digitizer. We began the experiment with a calibration of the detector using both ^{60}Co and ^{137}Cs. These data were taken with a 9.76mV trigger threshold. This allowed us to find our threshold in MeVee (MeV

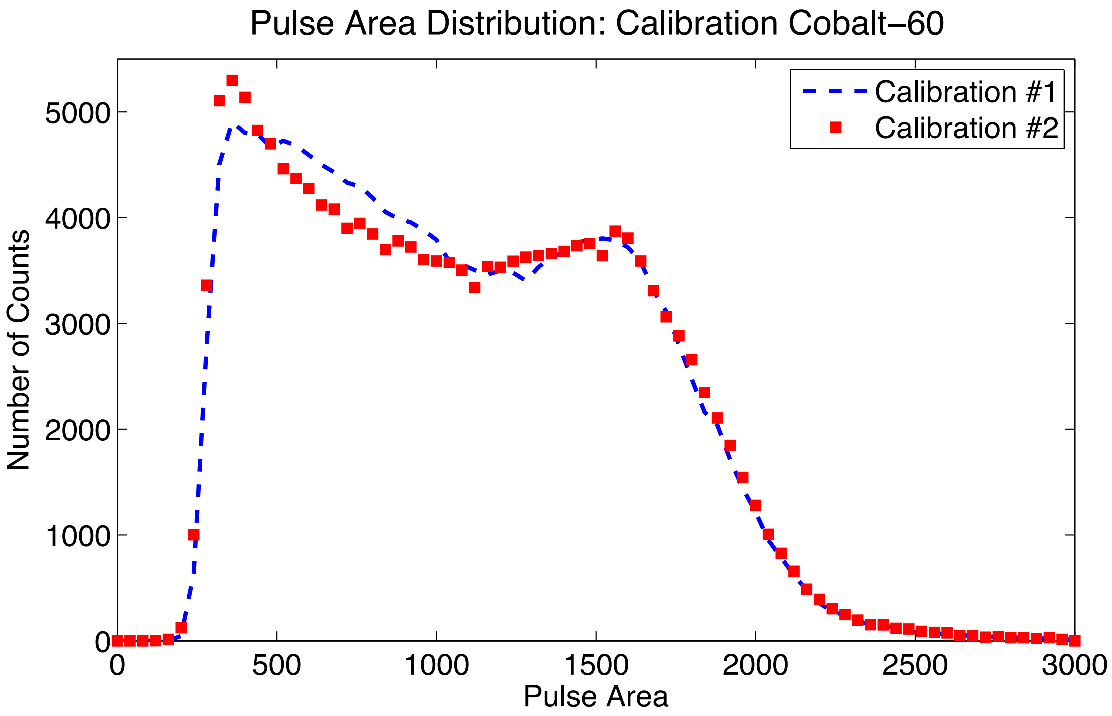

Figure 4.5 Two calibration runs using ^{60}Co, one at the beginning of the experiment and one after

electron equivalent), rather than merely in terms of millivolts. Also, by taking a second calibration at the end of the experiment, we were able to factor out any possible gain shifting. The second run was pure background, and lasted for 45 minutes. The next two runs were foreground with the ^{252}Cf source placed 12.15” from the face of the detector. Each run was 45 minutes in length, with a trigger threshold of 4.88mV and an acquisition window of 32μs.

4.3 Results

The pulse area distributions for cesium and cobalt calibration runs are shown in Figs. 4.5 and 4.6 respectively. Table 4.1 summarizes the data required to measure the threshold for the calibration runs and the background and foreground runs.

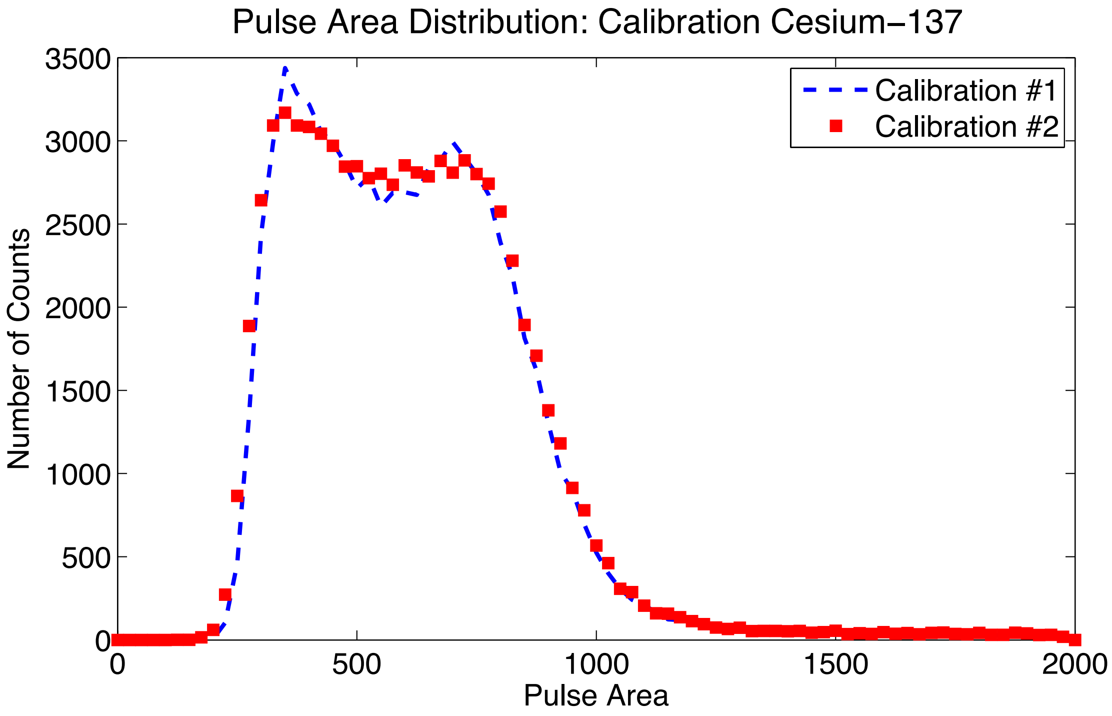

Figure 4.6 Two calibration runs using ^{137}Cs, one at the beginning of the experiment and one after

Source	Half-way Down Compton Edge	Half-way Down Threshold Edge	Threshold: 9.76mV trigger
^{137}Cs	89.35 channels	267.59 channels	143 keVee
^{60}Co	1916.47 channels	267.92 channels	145 keVee

Table 4.1 Calibration measurements and the consequent threshold calculations

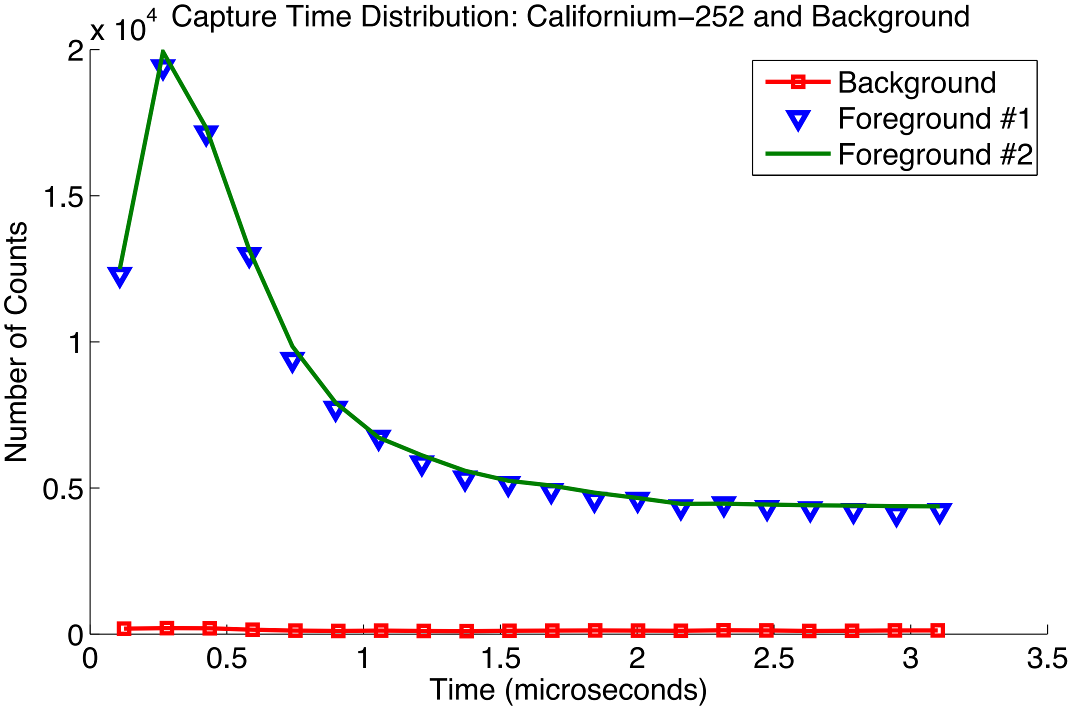

Figure 4.7 Three capture time distributions for the Cd detector, two foreground for ^{252}Cf and one background run

The results for the background run and foreground runs with ^{252}Cf are shown below in Fig. 4.7. Note that each of the three runs was for the same amount of time. The results of the late-time accidental calculation are summarized in Table 4.2. Note that in this table the background subtraction has already taken place for each foreground run. Also, the last five bins in the distribution were used, which corresponds to dual pulses separated by more than 24μs.

The ^{252}Cf source was calibrated at 23.78 μCi on April 15, 2008. SF represents 3.09% of the disintegrations, with 3.757 neutrons per fission. On July 24, 2011 the rate was 42,390 neutrons per

Run	Total DPS	Late-time Accidentals	Total Real DPS	Intrinsic Efficiency
Foreground #1	143,587	82,396	61,191	5.21%
Foreground #2	147,241	85,580	61,661	5.25%

Table 4.2 Calibration measurements and the consequent threshold calculations

second. The geometrical setup gave a $\frac{\Omega}{4\pi}$ of 0.01026. This means a rate of of 434.9 neutrons per second incident on the detector face.

4.4 Analysis and Discussion

The calibration runs went smoothly, with both runs for each source producing very similar pulse area distributions, as expected. The most important feature is the threshold rise on the left and the Compton edge on the right. As can be seen in both calibration runs, these two curves are almost exactly identical for both cesium and cobalt. This provides us with an important threshold for our intrinsic efficiency calculations with MCNP.

It is important to analyze the efficiency measurement results in the light of equations 4.1-4.3. The averaged intrinsic efficiency for the two foreground measurements is 5.23%. Using MCNP-PoliMi [1], the theoretical value for F_T, the fraction of neutrons that left a pulse above the 72 keVee threshold, is 45.8%, and F_C, the fraction of those neutrons that capture, is 26.3%. This gives a product of 11.56% of all neutrons make a measurable start pulse and capture in the cadmium. Consequently, the deduced value for E_γ, the efficiency of detecting the decay gammas from cadmium neutron capture, is 43.4%.

As mentioned before, the quantity E_γ is impossible to directly measure experimentally, and extremely challenging to calculate theoretically. Therefore, this measurement is our only estimate of this quantity. Fortunately, this value depends on a host of parameters, most important of which is volume of the detector. Consequently, building larger volume detectors could greatly increase the intrinsic and absolute efficiency of the detector system.

Overall, the cadmium-capture-gated detector system shows promise as a replacement for ^{3}He, especially as the detector volume approaches the size of traditional portal monitors. If a suitable alternate metal can be found with an electron energy distribution similar enough to that of cadmium, then the detector can function without the fear of extremely active sources causing accidental dual pulse signatures and thus, false alarms. The addition of a secondary detector that is neutron insensitive provides a method that reduces the effective gamma sensitivity of the detector system to levels acceptable for the U.S. Department of Homeland Security.

Chapter 5

Conclusions and Future Work

A neutron detector utilizing the capture-gated method was built and characterized. The detector's unique geometry and materials introduced many variables not present in a detector made of a single material. The effect of these variables was calculated with Monte Carlo techniques and measured monoenergetic and quasi-monoenergetic gamma sources and the electron energy distribution they created in the detector.

Furthermore, we introduced a suitable system for which to employ the detector in applications involving national defense/homeland security. This system has yet to be tested completely as we have yet to find a neutron-capture-insensitive metal with an identical Compton electron energy distribution to that of cadmium. Future work will focus on this, as such a system provides a method of subtracting accidental double pulse signatures caused not by background but by very active radioactive sources. An alternative method was used for calculating the intrinsic (and thus absolute) efficiency of the detector. This was done using a spontaneous fission neutron source. This alternative method is inferior to the ideal method proposed if the detector is to be accepted as a ^{3}He replacement.

Future work will also include larger-volume detectors. It is projected that this will greatly enhance the efficiency of the detector. Work is already in progress in developing detectors that are roughly four times the volume of the detector studied in this paper. Further work will also be done to decrease the lower threshold on the start pulse of the detector. This is important for applications where low-energy neutrons are of greatest interest.

Bibliography

[1] S. A. P. et. al., "MCNP-PoliMi: a Monte-Carlo code for correlation measurements," NIMA **513,** 550–558 (2003).

[2] T. Feder, "US Government Agencies Work to Minimize Damage to ^{3}He Shortfall," Physics Today **62,** 21–23 (2009).

[3] G. F. Knoll, *Radiation Detection and Measurements*, 3rd ed. (American Institute of Physics, Wiley, New York, 2000).

[4] P. N. N. Laboratories, *MCNP - A General Monte Carlo N-Particle Transport Code*, v3 and 4 ed. (University of California 1, 2003).

[5] E. Fermi, *Nuclear Physics*, revised edition ed. (The University of Chicago Press, Chicago, 1950).